The Astrophysical Journal Supplement Series, 145:199–211, 2003 April

AN OPTICAL SPECTROSCOPIC ATLAS OF LOW-REDSHIFT ACTIVE GALACTIC NUCLEI[1]

P. Marziani,[2] J. W. Sulentic,[3] R. Zamanov,[2] M. Calvani,[2] D. Dultzin-Hacyan,[4]
R. Bachev,[3] and T. Zwitter[5]

Received 2002 September 26; accepted 2002 November 8

ABSTRACT

We present a spectral atlas of the Hβ region for 215 type 1 AGNs (luminous Seyfert 1/radio galaxy nuclei and low-z quasars) up to $z \approx 0.8$. Line profiles and measures were derived from the database of intermediate resolution spectra ($R \gtrsim 1000$) with average continuum level S/N ratio $\approx$30. Parameters including rest frame equivalent width and FWHM are provided for the Fe II$_{opt}$ blend at λ4570, Hβ, He II λ4686, and the [O III] $\lambda\lambda$4959, 5007 emission lines. We extract clean broad component Hβ profiles and provide wavelength measurements at 0, 1/4, 1/2, 3/4, and 0.9 peak intensity levels in order to permit a quantitative definition of the Hβ broad component for statistical studies. We also discuss sources of uncertainty, selection effects, and biases in our sample. The data are especially important for tests of the eigenvector 1 parameter space occupation and correlation. We show that the I Zw 1 template Fe II$_{opt}$ spectrum reproduces well the observed Fe II$_{opt}$ emission for a wide range of line width and strength. A detailed analysis of the data within the eigenvector 1 context is deferred to a companion paper.

Subject headings: atlases — galaxies: active — galaxies: nuclei — quasars: emission lines — quasars: general

On-line material: additional figures, machine-readable tables

1. INTRODUCTION

Important information about the broad line emitting region (BLR) in active galactic nuclei (AGNs) can be extracted from observations of the Hβ spectral region. A wavelength coverage of $\approx$1000 Å allows one to measure, in addition to Hβ, the prominent Fe II$_{opt}$ low-ionization emission blends usually denoted as Fe II λ4570 and Fe II λ5300, the narrow [O III] $\lambda\lambda$4959, 5007 forbidden lines, and the high-ionization (HIL) He II λ4686 line at λ4686. These spectral features provide measures that constrain models of the two main structural components in AGNs:

1. the broad-line region (BLR), which is likely composed of two distinct emitting regions, at least in a large fraction of radio-quiet (RQ) AGNs: (*a*) a low-ionization line (LIL) emitting region (e.g., Balmer lines and Fe II$_{opt}$) and (*b*) an HIL emitting region associated with He II λ4686 and C IV λ1549 emission; Gaskell 1982; Collin-Souffrin et al. 1988; Marziani et al. 1996; Sulentic, Marziani, & Dultzin-Hacyan 2000a);
2. the narrow-line region (NLR), which has been resolved in the nearest AGN but whose structure and evolution remain unclear for the vast majority of luminous Seyfert 1 galaxies and for all quasars (see, e.g., Bennert et al. 2002; Zamanov et al. 2002).

Statistical studies offer the best hope for identifying evolutionary and structural changes among AGNs. Information on line profiles of moderately large samples of AGNs, and especially, comparison between lines emitted by ions of widely different ionization potential, have provided insights into the BLR structure (e.g., Marziani et al. 1996). This information is gaining new astrophysical significance following development of the eigenvector 1 parameter space (Sulentic et al. 2000a, 2000c; Boroson 2002).

In this paper, we follow a data analysis approach already successfully applied in several other studies. We describe the instrumental setups that we employed for the Hβ spectral range observations (§ 2) and introduce our sample of luminous Seyfert 1 and low-redshift quasars (§ 3). We discuss a number of biases that affect our sample. We then present the procedures followed in order: (i) to obtain reliable measurements of the heavily blended Fe II$_{opt}$ emission, and (ii) to properly clean Hβ of contaminating lines (§ 4.1). The continuum subtracted line emission and the uncontaminated Hβ broad component profiles are shown in the spectral atlas. Considering the sample size and its interest for statistical studies, special care was devoted to a reliable assessment of measurement errors (§ 4). We finally analyze briefly objects for which we have repeated observations available and point out new objects whose Hβ_{BC} profile may be variable (§ 5.3). The results of measurements and the associated errors are provided in digital format. The sample presented here was already used to calculate average spectra in the eigenvector 1 context (Sulentic et al. 2002) and to search for objects with large shifts between Hβ and [O III] λ5007 (Zamanov et al. 2002). In a companion paper, we will analyze the major implications for BLR structure. In another related paper, we will make use of this data set for studying the relationship between several low-redshift BAL QSOs in our sample and the general AGN population. In the future, the atlas will provide a reference for any eventual spectral change, especially those of the profile of the Hβ broad component (Hβ_{BC}). The highest S/N spectra can be used for a more thorough analysis of Fe II$_{opt}$ multiplet ratios.

[1] Based in part on data collected at ESO La Silla.

[2] INAF, Osservatorio Astronomico di Padova, Vicolo dell'Osservatorio 5, I-35122 Padua, Italy; marziani@pd.astro.it, calvani@pd.astro.it, zamanov@pd.astro.it.

[3] Department of Physics and Astronomy, University of Alabama, Tuscaloosa, AL 35487; giacomo@merlot.astr.ua.edu.

[4] Instituto de Astronomía, UNAM, Apartado Postal 70-264, 04510 Mexico D.F., Mexico; deborah@astroscu.unam.mx.

[5] Department of Physics, Univerza Ljubljani, Jadranska 19, SI-1000 Ljubljana, Slovenia; tomaz.zwitter@uni-lj.si.

2. OBSERVATIONS

Spectra were obtained with very similar instrumental setups yielding resolution in the range 4–7.5 Å FWHM. The median value of the S/N of our spectra is ≈25. Figure 1 shows the distribution of S/N values for our sample. We use the value for an average spectrum in the case of sources with multiple spectra of comparable quality. Spectra were obtained with the following telescopes and spectrographs: ESO 1.5 m (B&Ch), San Pedro Martir 2.2 m (B&Ch), Calar Alto 2.2 m (B&Ch), KPNO 2.2 m (Gold), and Asiago 1.82 m (B&Ch). Results based on analysis of parts of this sample can be found in Sulentic et al. (1995), Marziani et al. (1996), and Sulentic et al. (2000a, 2002c). The observations span 12 years. Format and especially efficiency of CCD have both increased, albeit not dramatically so and in way that has not strongly influenced the feasibility of our project (even the smallest CCD allowed a coverage of ≈1500 Å).

Table 1 summarizes the instrumental setup for each observing run during which we obtained useful data. Data are organized as follows:

Column (1).—Observing run code.

Column (2).—Identification of the observing site.

Column (3).—Telescope aperture.

Column (4).—Observing dates.

Column (5).—Spectrograph.

Column (6).—Dispersion in Å mm^{-1}.

Column (7).—Detector (always CCD) format in pixels.

Column (8).—CCD manufacturer.

Column (9).—Slit width on the sky plane used for science exposures.

Column (10).—Spectral resolution at FWHM measured on the instrumental profile (identified by weak comparison spectrum lines).

The data are supplemented by several spectra kindly provided by T. Boroson (identified as BG in Table 1) and M.-H. Ulrich (ESOOct95). The data of the ESOOct95 run have not been published previously and were reduced by one of the authors. Several of the observing runs were motivated by (1) the study of objects with strong He II λ4686 emission and (2) the observations of $H\beta_{BC}$ line profile, either to match to C IV λ1549 observations available from the *Hubble Space Telescope* (*HST*) or to identify and study peculiar $H\beta_{BC}$ line profiles. Unpublished observations cover ≈70% of the sample objects considered in this work.

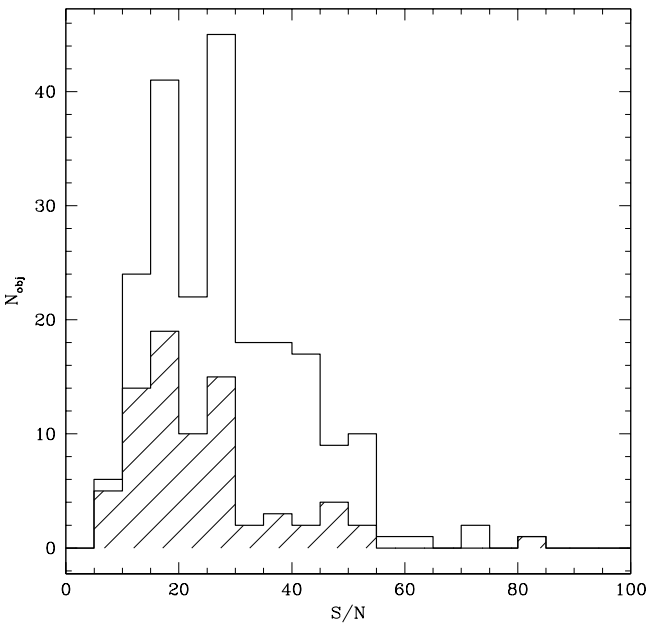

FIG. 1.—Distribution of S/N ratio for the 215 spectra employed in this paper and shown in Fig. 4. The dashed histograms refer to radio-loud objects.

Table 2 provides a log of observations that is organized as follows:

Column (1).—IAU source designation.

Column (2).—Common name.

Column (3).—Redshift z, as reported in the catalog by Véron-Cetty & Véron (2000). In the case of 12 objects, when the cataloged redshift disagrees by more than $|\Delta z| \approx 0.003$, either (1) we substitute the cataloged value with our determination if we have more than one spectrum (or if there is a published value) or (2) we report in a footnote our independent estimate if we have one spectrum and no other reliable source of control).

Column (4).—Apparent V magnitude, also from Véron-Cetty & Véron (2000).

Column (5).—Specific flux at 6 cm in Jy, always from Véron-Cetty & Véron (2000).

Column (6).—Absolute B magnitude computed by Véron-Cetty & Véron (2000).

Column (7).—Observing date.

Column (8).—Universal Time (UT) at exposure start in the format hh:mm.

Column (9).—Total exposure time in seconds (summing up subsequent exposures with same setting).

2.1. *Calibrations and Instrumental Errors*

Wavelength calibration was achieved by observation of comparison spectra usually obtained after an exposure (if single) or between exposures (if two or more consecutive exposures were taken), with the telescope till pointing toward the target. Wavelength calibration was accomplished by fitting a polynomial of suitable order to the pixel-wavelength correlation. Residuals were always $\lesssim 0.1$ Å rms (corresponding to ∼5 km s^{-1} at $H\beta$), and the calibration was compared with a sky line spectrum extracted from the science frame to avoid errors associated to small shifts between the science frame and the comparison.

Slit width was typically 1″.5–2″. This resulted from the usual trade-off between preserving spectral resolution and minimizing light losses due to seeing and differential refraction. It was not always possible/time effective to align the slit along the parallactic direction. Sky conditions were not always photometric during a number of observations.

We compared the apparent magnitude deduced from our spectra with the apparent m_V tabulated by Véron-Cetty & Véron (2000). The distribution is displaced by $\Delta m_V \approx -0.4$. The distribution of Δm_V is also skewed toward large negative values. These systematic effects are expected due to the narrow slit aperture usually employed. The dispersion is rather large, $\sigma \approx 0.64$, and it is most likely affected also by the heterogeneous origin of the catalog magnitudes. We have flagged observations that *may* have suffered extraordinary light losses and that should therefore be regarded as completely nonphotometric (due to e.g., thick clouds, seeing, differential refraction) if they are fainter than $\Delta m_V \gtrsim -1.5$ with respect to the tabulated magnitudes.

TABLE 1

SYNOPSIS OF OPTICAL SPECTROSCOPY

Obs. Run Code (1)	Observatory (2)	Dates (3)	Tel. Apert. (m) (4)	Spectr. (5)	Disp. (Å mm^{-1}) (6)	Detector		Slit Width (arcsec) (9)	Sp. Res. (Å) (10)
						Format (7)	Manufacturer (8)		
SPMJun01	OAN, San Pedro Martir	2001 Jun 22–25	2.1	B&Ch	86	1024^2	SITe	2.6	3–4
ESOOct96	ESO, La Silla	1996 Oct 11–13	1.5	B&Ch	118	2048^2	Loral	1.8	3
SPMMay96	OAN, San Pedro Martir	1996 May 18–21	2.1	B&Ch	86	1024^2	Tektronik	2.6	≈6.5
ESOOct95	ESO, La Silla	1995 Oct 27–29	2.2	EFOSC2	67	1024^2	Thomson	1.0	7.5
SPMJun95	OAN, San Pedro Martir	1995 Jun 27–30	2.1	B&Ch	86	1024^2	Tektronik	2.6	4.5
SPMDec94	OAN, San Pedro Martir	1994 Dec 9–13	2.1	B&Ch	125	1024^2	Tektronik	2.6	7
CAApr94	MPIfA, Calar Alto	1994 Apr 6–9	2.2	B&Ch	114	1024^2	Tektronik	2.0	5.8–8.0
SPMNov93	OAN, San Pedro Martir	1993 Nov 18–21	2.1	B&Ch	132	1024^2	Tektronik	2.6	5.0
ESODec93	ESO, La Silla	1993 Dec 17–22	1.5	B&Ch	132	2048^2	Ford Aerospace 2K	2.0	4.2
ESOMay93	ESO, La Silla	1993 May 20–24	1.5	B&Ch	132	2048^2	Ford Aerospace 2K	2.0	4.2
BG	Kitt Peak Nat. Obs.	1991 Apr 21–24	2.1	Gold	165	800^2	Texas Instruments	1.5	6.5–7
KPNOFeb91	Kitt Peak Nat. Obs.	1991 Feb 18–21	2.1	Gold	≈60	800^2	Texas Instruments	2.5	3.2
KPNOOct90	Kitt Peak Nat. Obs.	1990 Oct 16–18	2.1	Gold	≈60	800^2	Texas Instruments	2.5	3.2
BG	Kitt Peak Nat. Obs.	1990 Oct 10–11	2.1	Gold	165	800^2	Texas Instruments	1.5	6.5–7
BG	Kitt Peak Nat. Obs.	1990 Sep 15–20	2.1	Gold	165	800^2	Texas Instruments	1.5	6.5–7
BG	Kitt Peak Nat. Obs.	1990 Apr 21–23	2.1	Gold	165	800^2	Texas Instruments	1.5	6.5–7
ESOApr90	ESO, La Silla	1990 Apr 1–4	1.5	B&Ch	128	1024^2	RCA	1.5	3.5
BG	Kitt Peak Nat. Obs.	1990 Feb 15–20	2.1	Gold	165	800^2	Texas Instruments	1.5	6.5–7
ESOSep89	ESO, La Silla	1989 Sep 25–29	1.5	B&Ch	128	1024^2	RCA	1.5	3.5
AsMar89	Asiago	1989 Mar 23–27	1.8	B&Ch	≈120	580	Thompson	2.5	5.5

TABLE 2
OBJECT IDENTIFICATION AND LOG OF OPTICAL OBSERVATIONS

IAU Code Name (1)	Common Name (2)	z (3)	m_V (4)	F(6 cm) (Jy) (5)	M_B (6)	Date (7)	U.T. (8)	Exposure Time (s) (9)
J00059+1609	PKS 0003+15	0.450	16.4	0.340	−25.7	1996 Oct 14	04:02	3600
J00063+2012	Mrk 335	0.025	13.9	0.003	−21.7	1996 Oct 13	04:02	3000
J00105+1058	III Zw 2	0.090	15.4	0.435	−22.7	1994 Oct 08	02:07	3600
J00196+2602	4C 25.01	0.284	15.5	0.483	−25.8	1990 Oct 18	03:47	1800
J00292+1316	PG 0026+12	0.142	15.4	0.002	−24.0	1990 Oct 11	08:34	3000
J00457+0410	PG 0043+039	0.385	16.0	0.000	−26.0	1990 Sep 20	05:44	2700
J00470+0319	PKS 0044+030	0.624	16.4	0.069	−26.6	1994 Dec 13	02:37	3600
J00495+1128	PHL 850	0.275	17.1	0.001	−24.1	1990 Oct 18	04:27	5400
J00519+1725	Mrk 1148	0.064	16.0	0.001	−21.5	1990 Sep 18	06:49	1800
J00535+1241	I Zw 1	0.061	14.0	0.003	−23.4	1994 Oct 07	04:11	3600

NOTE.—Table 2 is available in its entirety in the electronic edition of the *Astrophysical Journal Supplement*. A portion is shown here for guidance regarding its form and content.

Three objects (J01032+0221, J04136+1112, J06300+6905, all of them of run SPMNov93) were not reduced to an f_λ scale, although otherwise corrected for instrumental response and atmospheric losses. We remark that catalog magnitudes may be also subject to large errors. At least one object (J08045+6459) has a S/N ratio that is more consistent with a 14–15 mag object and not with the cataloged value $m_V \approx 17.5$.

A tentative estimate of our flux scale uncertainty is ±50%. We report the f_λ values since they retain a statistical value but should be considered with care in case individual objects are considered.

3. SAMPLE PROPERTIES

Figure 2 shows the distribution of redshift, absolute B magnitude, apparent magnitude, and Kellermann's R ratio for our sample. The shaded part of the histograms indicate the radio-loud (RL) subsample. The quantity R is defined as the ratio between the flux density at 6 cm and 4400 Å (B band; Kellermann et al. 1989). All the data have been retrieved from the 9th edition of the Véron catalog (Véron-Cetty & Véron 2000). Note that the histogram of radio-loudness measures includes only those radio-quiet (RQ) sources with a radio detection. Many RQ nondetections or unobserved sources are not shown there.

Figure 2*a* shows that our sample is strongly biased toward the lowest redshift type 1 AGNs. Expansion of the sample in the range $z \approx 0.2$–0.8 cannot be accomplished with 2 m class telescopes without sacrificing resolution and/or S/N. Data of lower quality cannot provide an effective test of the eigenvector 1 concept and, in fact, blur the differences between all classes of AGNs. Even our measures of Fe II λ4570 strength for these bright sources cannot completely define E1 source occupation and correlation at the low end of the $R_{\rm Fe\ II}$ range where only upper limits can be assigned (see Sulentic et al. 2002 and § 4.2). The distribution of source apparent magnitude shown in Figure 2*b* reflects the constraint imposed by 2 m class telescope. It suggests that we have effectively sampled AGNs brighter than $m_V \approx 16.0$. Fortunately, even this bright apparent magnitude cutoff includes some reasonably luminous AGNs. The result is that we uniformly sample 3 orders of magnitude in source luminosity as can be seen in Figure 2*c*.

Another important bias involves RL sources which favor higher redshift and source luminosity than the RQ AGNs in our sample. This reflects both operational and physical biases. The RL expectation for low-z samples is ≈10% (Urry & Padovani 1995; Hooper et al. 1995). It is unclear if the most complete low-redshift (PG) sample is over-represented with RL sources (17/87) or whether distant samples are RL deficient (Sulentic et al. 2000a, 2000c; Marziani et al. 2001). The *HST* archive is certainly over-represented with RL sources (with C IV λ1549 spectra; Marziani et al. (1996) had 60% of 52 sources that were radio loud!). Our present, final sample of $n = 215$ sources is also RL over-represented ($n = 77$; ≈36%). Certainly our distinction between different AGN spectral types (Sulentic et al. 2002) and, especially, between populations A and B, i.e., pure RQ AGNs with FWHM($H\beta_{\rm BC}$) ≤ 4000 km s^{-1} and mixed RQ/RL AGNs with FWHM($H\beta_{\rm BC}$) ≥ 4000 km s^{-1}, respectively (Sulentic et al. 2000a, 2000b, 2000c), does not imply that one can infer information on the relative frequency of each population.

4. DATA ANALYSIS

4.1. *Data Processing*

The following processing steps were applied to the data.

1. The spectra were deredshifted using measurements of $H\beta_{\rm NC}$ (and in a few cases in which $H\beta_{\rm NC}$ was not well defined, of [O III] λ5007).

2. The local continuum in the Hγ–Hβ spectral range (≈4200–5600 Å) was approximated using regions around 4200, 4700, and 5500 Å that are relatively unaffected by Fe $II_{\rm opt}$ emission. The objects of our sample are all luminous AGNs, and the aperture on the cross-dispersion profile was chosen to avoid to isolate the nuclear spectrum only. We did not notice appreciable contamination by the host galaxy spectrum.

3. The Fe II λ4570 complex was subtracted using the template method of Boroson & Green (1992; see also Marziani et al. 1996). The method is described in detail in § 4.2.

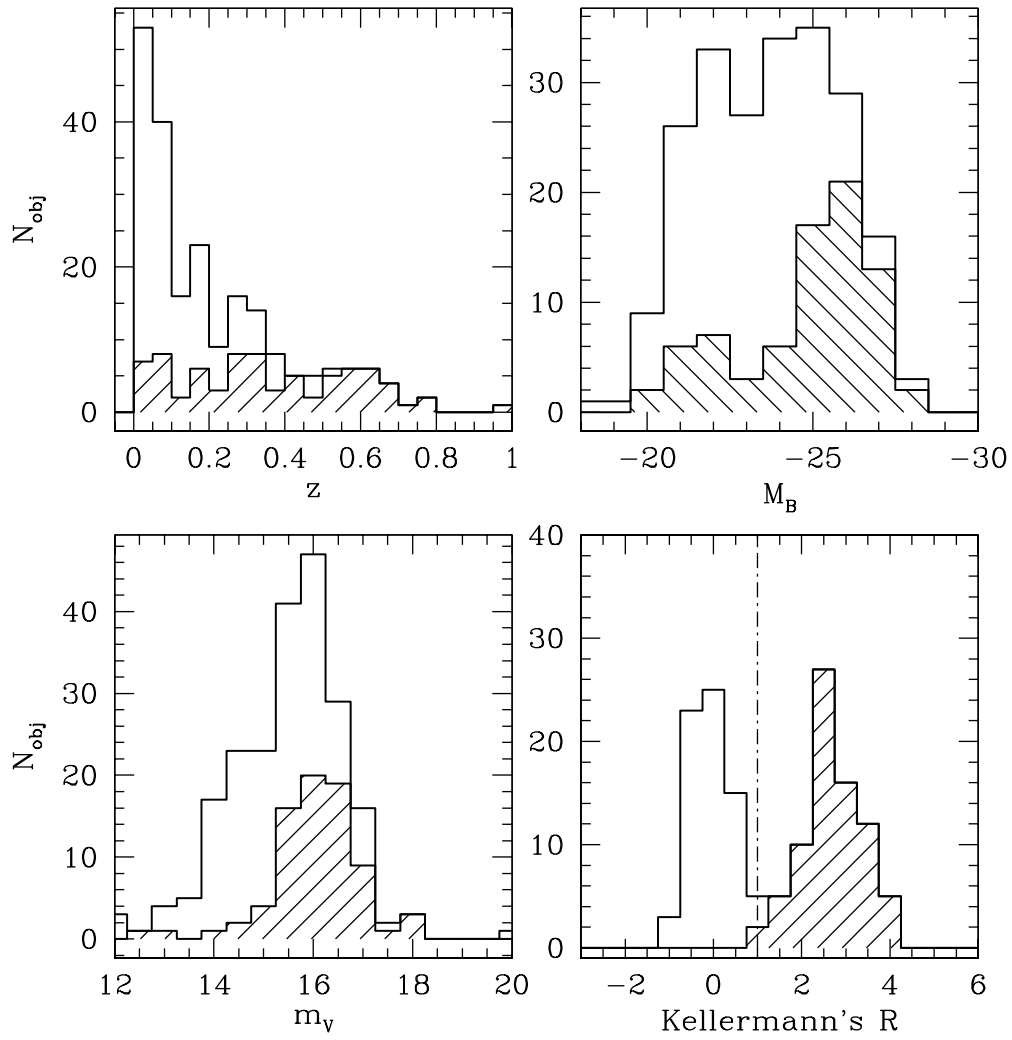

FIG. 2.—Distribution of redshift, absolute B magnitude, apparent V magnitude, and Kellermann's R for the 215 objects of our sample. The dashed histograms refer to radio-loud objects.

4. Emission lines of [O III] λ4959 and [O III] λ5007 were subtracted by interpolating between the blue and red wings of these features or by subtracting multiple Gaussians.

5. The broad and narrow component of the He II λ4686 line were subtracted (whenever it was detected) by using a Gaussian fit (note that this procedure *assumes* a symmetric profile for the broad component of He II λ4686).

6. The narrow component of Hβ was subtracted using a Gaussian profile (see § 4.3 for more details).

7. We fitted a high-order spline function to the cleaned H$\beta_{\rm BC}$ profile from which we measured the wavelength $\lambda_B(i/4)$ and $\lambda_R(i/4)$ at fractional intensities $i/4$, for $i = 0$, 1, 2, and 3. We do not provide any $\lambda_{\rm Peak}$, since it is too much affected by H$\beta_{\rm NC}$. Instead we provide $\lambda_B(9/10)$ and $\lambda_R(9/10)$.

4.2. Fe II λ4570 *Measurements*

Measures of the Fe II$_{\rm opt}$ emission appear to be an important parameter for distinguishing between different AGN classes. Right now our ability to maximize the "dynamic range" of the E1 parameter space is limited by the accuracy of Fe II$_{\rm opt}$ measurements. We use an Fe II$_{\rm opt}$ template that is derived from I Zw 1 and is almost identical to the original template of Boroson & Green (1992), although based on a spectrum of higher resolution and wider wavelength coverage. An estimate of FWHM for the Fe II λ4570 lines was obtained using the template and Gaussian smoothing by an appropriate "broadening factor." Since our template was derived from I Zw 1, we cannot properly estimate line widths lower than those of the template, which is FWHM $\approx$ 1100 km s^{-1}. Only a few "narrow-line" Seyfert 1 (NLSy1) sources should fall in that category.

Measurement of W(Fe II λ4570) (integrated over the range 4434–4684 Å) and of the broadening factor were accomplished by constructing an array of template spectra within reasonable limits of scaling and broadening factors. We then obtained the best scaling and broadening factors for each continuum-subtracted spectrum by subtracting the templates and by identifying the one template that minimized the sum of the least-square residuals in the range 4450–4600 Å. Errors were estimated by identifying the nearest templates in the array that produced significantly larger residuals. While this procedure allowed us to identify the best template fit in a rigorous way, the method for estimating uncertainties was rather subjective. In several cases with

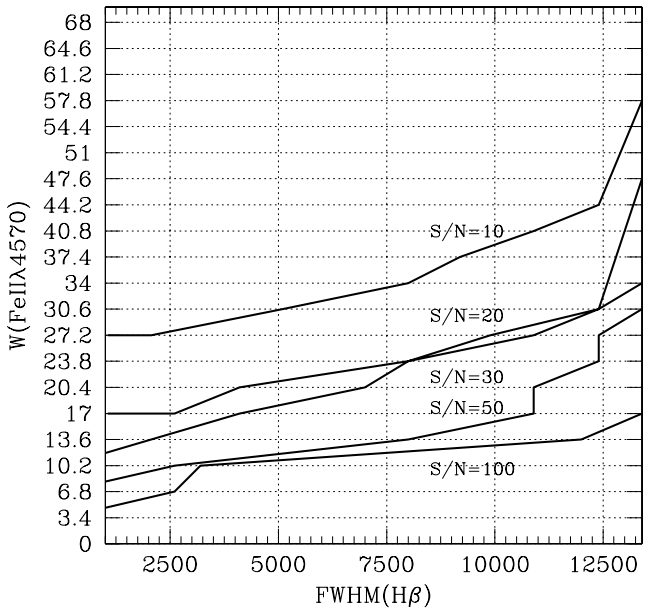

FIG. 3.—Minimum detectable W(Fe II λ4570) as a function of FWHM(Hβ_{BC}) for five different S/N values (10, 20, 30, 50, and 100).

strong [W(Fe II λ4570) $\gtrsim$ 30 Å] emission, it was necessary to iterate by first performing a tentative Fe II$_{opt}$ subtraction in order to identify the underlying continuum followed by a second iteration after continuum subtraction to obtain the actual Fe II λ4570 measures.

The detection of Fe II$_{opt}$ depends on S/N and on the width of the individual lines (assumed to be the same as Hβ). Unfortunately, Fe II$_{opt}$ emission is heavily blended, and if the lines are broad enough, they become increasingly difficult to detect at a given S/N ratio. $R_{Fe\ II}$ values reported in the literature are also influenced by an historical bias, first because the occurrence of Fe II$_{opt}$ emission was not well appreciated (especially when nonlinear detectors such as photographic plates were in use), and second because it was widely believed that Fe II$_{opt}$ emission was ubiquitous among AGNs. We now know that Fe II$_{opt}$ emission varies systematically across the E1 sequence, and we know which AGNs can be expected to show strong or weak Fe II$_{opt}$ emission. However, there is still a danger related to the subjective evaluation of a spectrum. In order to minimize subjective bias, we created artificial AGN spectra with a typical AGN continuum and Hβ, Fe II$_{opt}$ + [O III] $\lambda\lambda$4959, 5007 emission lines. We varied the strength and width of Hβ and Fe II$_{opt}$ emission (assumed to have equal FWHM) for five different S/N ratio values (10, 20, 30, 50, and 100). Using the simulated spectra, we visually estimated the minimum detectable Fe II$_{opt}$ [quantified as W_{min}(Fe II λ4570)]. The results are shown in Figure 3. Note that the lines of Figure 3 identify the minimum detectable value, so that a proper upper limit should be set at ΔW(Fe II λ4570) $\approx$ 4 Å less. Only in the case W(Fe II λ4570) $> W_{min}$(Fe II λ4570), was it possible to obtain an appropriate "broadening factor" which defines the width of the Fe II$_{opt}$ lines.

4.3. *Hβ Measurements*

FWHM(Hβ) was initially measured interactively with the SPLOT task of IRAF, and eventually using an automated FORTRAN program employed to measure the Hβ_{BC} line parameters (see § 5.2). This enabled us to compare two independent sets of measures for the same data. The comparison was highly useful for identifying sources with the most peculiar profiles. There was strong agreement between the two sources of measures for most sources (ΔFWHM$\sim$ 50 km s^{-1}). This difference can be entirely ascribed to the difficulty of placing the cursor rigorously at half-maximum while measuring the spectrum interactively. FWHM(Hβ_{BC}) appears to be a fairly robust measurement. Agreement between independent measures does not mean that one has a true measure of the "classical" broad-line component.

A reliable estimate of line properties and uncertainty must take into account that the Hβ_{BC} profile decomposition is complicated by several effects. The effects we identified include the following:

Continuum placement.—Uncertainty in continuum estimation, which depends on (*a*) adequate spectral coverage blueward of the λ4570 and redward of the λ5300 Fe II blends, (*b*) presence of a very broad He II λ4686 component, (*c*) presence of an extended Hβ_{BC} red wing, and, most importantly, (*d*) S/N, which makes the first three difficult to evaluate.

Hβ *VBLR component*.—The presence of a "very broad" line region (VBLR) component or red wing/shelf on the Hβ line. This feature sometimes extends redward of [O III] λ5007 and, more rarely, blueward of rest frame λ4650 (e.g., RXJ 0204−51; Grupe et al. 1999). This problem should be restricted to E1-defined RQ population B and RL sources (Sulentic et al. 2000c, 2002). In some sources the VBLR component may be the only broad-line component present (see, e.g., Sulentic et al. 2000b). The VBLR component is usually redshifted and typically twice as broad as FWHM of the classical broad component ($\sim$10,000 km s^{-1}). Inclusion or exclusion of the VBLR component will have a very large effect on measures of equivalent width and FWHM Hβ. In noisy spectra the continuum is often fitted on top of the VBLR component.

Hβ_{NC} *component*.—Subtraction of a narrow-line Hβ component, which was done according to the following criteria:

1. If a clear inflection is seen, the subtraction is trivial. This is the case of most sources.
2. In the cases where an inflection is not seen, we subtracted a Gaussian profile under the condition that FWHM(Hβ_{NC}) = FWHM([O III] λ5007).
3. This last condition is not always applicable. For several population A sources (e.g., NLSy1's) with typically Lorentzian profiles and FWHM $<$ 4000 km s^{-1} the inflection is not observed. We have not subtracted an NLR component in population A sources unless an inflection was observed. There are seven sources with such property. We found, a posteriori, an intriguing result: the seven sources are "blue-outliers," i.e., objects for which the recessional velocity measured on [O III] λ5007 is lower than that of Hβ_{NC} by more than 250 km s^{-1} (Zamanov et al. 2002). *Only* in such cases is there really no hint at an inflection. [O III] $\lambda\lambda$4959, 5007 is unusually broad as well. We remark that the spikelike appearance of the Hβ profile core is consistent with the interpretation of these objects pointed out by Zamanov et al. (2002): objects seen along or close the symmetry axis of a high-ionization line outflow, with Hβ_{BC} emission due to a flattened gas distribution (possibly an accretion disk) seen face-on.

The lack of certainty about the existence and strength of the narrow component can otherwise strongly affect FWHM and EW measures. A case in point involves I Zw 1, where FWHM $\approx$ 1200 km s^{-1} without an H$\beta_{\rm NC}$ component subtraction but can be as large as 4500 km s^{-1} with a subtraction based on typical narrow-line widths (Marziani et al. 1996). Since such profiles rarely show an inflection, there is no a priori indicator of H$\beta_{\rm NC}$ strength. Subtraction of a significant narrow component in many of these sources would imply H$\beta_{\rm NC}$ stronger than or comparable with [O III] λ5007, which is not consistent with other forbidden line ratios (Nagao, Murayama, & Taniguchi 2001). Typically, H$\beta_{\rm NC}$ is $\approx$1/10 the strength of [O III] λ5007. In the outliers, any H$\beta_{\rm NC}$ would be appreciably displaced along the H$\beta_{\rm BC}$ profile. However, since W([O III] λ5007) $\sim$ 2.5–15 Å, the H$\beta_{\rm NC}$ becomes too weak to be detected. This argues against the subtraction of a strong H$\beta_{\rm NC}$ in population A sources. We believe that our approach is now entirely self-consistent. After the systematic effects we describe are taken into account, we think that any residual ambiguity in the definition of H$\beta_{\rm NC}$ will not affect relevant parameters above the stated uncertainty.

[O III] $\lambda\lambda$4959, 5007 *contamination*.—Another source of uncertainty includes weaker lines in the Hβ spectral range. Of particular relevance are "semibroad" [O III] $\lambda\lambda$4959, 5007 emission as well as (possibly) He I emission at λ4922 and λ5016 (Verón, Gonçalves, & Véron-Cetty 2002). The existence of semibroad [O III] λ5007 is a long-standing controversy. While the evidence for a semibroad component is weak (Zheng & Sulentic 1990), high-resolution studies of the [O III] lines show that it is frequently blue asymmetric (as often seen also in our spectra; see J06300+6905 for the most spectacular example). The [O III] λ5007 asymmetry may be a problem if the red wing H$\beta_{\rm BC}$ merges smoothly with [O III] λ5007. In this case measures of $\lambda_R(0)$ for H$\beta_{\rm BC}$ may be significantly affected. Without entering into the debate about the reality of any semibroad [O III] $\lambda\lambda$4959, 5007 emission, a blueward asymmetry is the most likely case, but [O III] $\lambda\lambda$4959, 5007 lines have been observed with redward asymmetry and multiple component profiles in spectra with resolution $R = \lambda/\Delta\lambda \gtrsim 1000$, i.e., at resolution comparable to many of our spectra. Therefore, we adopted an empirical approach with the [O III] $\lambda\lambda$4959, 5007 subtraction done by rigorously constraining the ratio I([O III] λ5007)/I(O III λ4959) $\approx 3.0 \pm 0.1$. Asymmetric profiles are markedly non-Gaussian, so care was taken to subtract self-similar profiles for both [O III] λ5007 and [O III] λ4959 by either interpolating below [O III] $\lambda\lambda$4959, 5007 with a straight line or applying a multi-Gaussian procedure.

Other weaker lines.—Any consideration about other contaminating lines can be done *after* Fe II$_{\rm opt}$ and O [III] $\lambda\lambda$4959, 5007 subtraction. Broad He I λ5016 emission would give rise to a broad red [O III] λ5007 wing (Véron et al. 2002). In special cases, the contamination by He I λ4922 and 5016 could give rise to a faint redward wing extending somewhat beyond the red side of [O III] λ5007, again affecting significantly the $\lambda_R(0)$ measurement. In order to estimate the effect of the He I lines on the H$\beta_{\rm BC}$ line profiles, we performed photoionization computations with CLOUDY (Ferland 2000). Population A and population B sources were modeled using different values for the ionization parameter and electron density: $\log U = -2$, $\log n_e = 11$ for population A, and $\log U = -1$, $\log n_e = 9.5$ for population B (Marziani et al. 2001). The case B intensity ratio is I(He I λ5016)/I(H$\beta_{\rm BC}$) $\approx$ 0.14 for population A and 0.035 for population B. An intermediate case with $\log U = -1.5$, $\log n_e = 10$ yields an intensity ratio 0.045. We conclude that He I emission cannot explain the prominent redward asymmetry in many population B objects and especially in average quasar spectra (Sulentic et al. 2002). We would expect He I to be more prominent in population A, and in borderline objects between population A and population B, such as J15040+1026. A telltale signature of that feature, after Fe II$_{\rm opt}$ subtraction, would involve a dip between [O III] λ5007 and [O III] λ4959 extending almost to the continuum level. In such cases, the "red shelf" of [O III] λ5007 cannot be assumed part of the H$\beta_{\rm BC}$ red wing (see for example J13130−1107). The worst cases are the ones in which the H$\beta_{\rm BC}$ red wing and any [O III] λ5007 red shelf merge smoothly, creating a relatively "flat" red extension to H$\beta_{\rm BC}$. Estimation of the red wing extent for H$\beta_{\rm BC}$ is somewhat arbitrary in such cases. However, this arbitrariness is usually taken into account by the errors given for $\lambda_R(0)$: everything below 5% fractional intensity is within the uncertainty (§ 5.2). More generally, the combined effect of H$\beta_{\rm NC}$ and continuum placement uncertainties are estimated to produce an effect on H$\beta_{\rm BC}$ line profile parameters that is mimicked by a $\pm$0.05 change in fractional intensity level.

4.4. He II λ4686

He II λ4686$_{\rm BC}$ was detected and measured in 109 sources. Adequate S/N ratio and resolution are both responsible for this high detection rate. However, since part of our sample is composed of sources selected for the presence of strong He II λ4686$_{\rm BC}$ emission, no inference about the relative frequency of occurrence can be made. FWHM(He II λ4686$_{\rm BC}$) was measured using a simple Gaussian fitting procedure that, in most cases, modeled the short-wavelength part of the profile which is less influenced by the broad component of Hβ. In spectra where the entire profile was visible we modeled the full profile and the short and long-wavelength parts separately. FWHM(He II λ4686$_{\rm NC}$) was also measured with a Gaussian fitting (and removed before He II λ4686$_{\rm BC}$ was fitted). It is worth noting that in most of our sources He II λ4686$_{\rm NC}$ and He II λ4686$_{\rm BC}$ can be clearly distinguished and that blending problems between BC and NC are never as severe as they can be for Hβ. Estimated uncertainties are approximately a factor of 2 if I(He II λ4686)/I(H$\beta_{\rm BC}$) $\approx$ 0.1; if I(He II λ4686)/I(H$\beta_{\rm BC}$) $\gtrsim$ 0.2, the uncertainty associated with W(He II λ4686) measures is estimated to be $\pm$20%. Typical uncertainty for FWHM(He II λ4686$_{\rm BC}$) (whenever this parameter is reported) is $\pm$20%.

5. RESULTS

5.1. *Spectral Atlas*

Figure 4 presents the atlas of spectra for our sample of 215 AGNs. The left panel for each spectrum shows the continuum subtracted Hβ spectral region extending from Hγ to the red end of the λ5300 Fe II$_{\rm opt}$ blend. This allows one to visually evaluate the intensity of the Fe II$_{\rm opt}$ emission, Hβ line width, as well as the strength of the He II λ4686 line. The adopted Fe II$_{\rm opt}$ template is superimposed as a solid line. The right panel for each spectrum shows the Hβ region after continuum and Fe II$_{\rm opt}$ subtraction. The H$\beta_{\rm BC}$ was derived by subtracting any additional contamination from He II λ4686, [O III] $\lambda\lambda$4959, 5007, and H$\beta_{\rm NC}$. The resultant

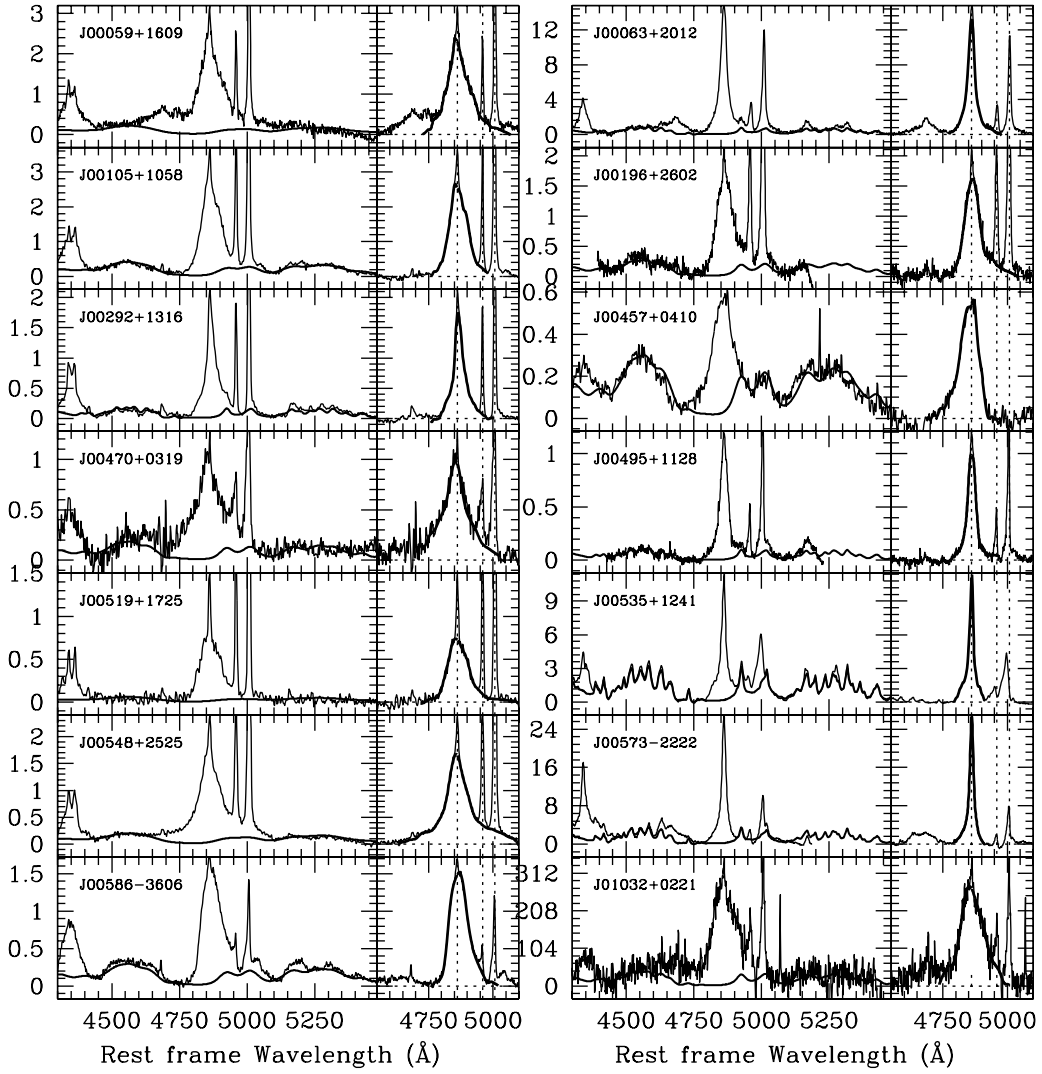

FIG. 4.—Spectral atlas of the 215 type 1 AGNs of this study. For 14 objects in each page the left panel shows the continuum subtracted Hβ spectral region. Abscissa is rest frame wavelength in Å, ordinate is specific flux in units 10^{-15} ergs s^{-1} cm^{-2} Å^{-1}. The best fit Fe II$_{opt}$ emission (see text) is traced as a thin green line. The right panel shows an expansion around Hβ of the same spectrum after continuum and Fe II$_{opt}$ subtraction. Abscissa and ordinate are in then same units. The blue and red thick line show a spline fitting of the pure Hβ_{BC} on the short- and long-wavelength side of the line, respectively. Note that the ordinate scale of J01032+0221, J04136+1112, and J06300+6905 is arbitrary. [*See the electronic edition of the Journal for a color version of this figure and additional parts to this figure*].

Hβ_{BC} was then fitted with a high-order spline function in order to minimize effects of noise while attempting to preserve the intrinsic complex shape (i.e., VBLR, double peaked structure, steep profile segments, etc.). We assumed that Hβ_{NC} (or the peak of Hβ for the narrower profiles) represents the best approximation of the AGN rest frame velocity. This is supported by a preliminary comparison between the CO and 21 cm measurements available for objects in our sample (Marziani et al. 1996, I Zw 1; Zamanov et al. 2002); note that [O III] $\lambda\lambda$4959, 5007 may show blueshifts up to ~ -1000 km s^{-1}). We make available (1) the original rest-frame spectra (not shown in the atlas), (2) the continuum-subtracted spectra; (3) the continuum and Fe II$_{opt}$ subtracted spectra, (4) the Fe II$_{opt}$ spectra assumed for each object.[6] All spectra are in ASCII format.

[6] Available at http://web.pd.astro.it/marziani/spect.tar.gr.

5.2. *Tabular Data*

Results on measurements are reported in Tables 3 and 4. All measurements of equivalent width, FWHM, and continuum specific flux are given in the AGN rest frame. The format of Table 3 is as follows:

Column (1).—IAU source designation.

Column (2).—S/N in the continuum, measured in spectral regions free of emission lines and before Fe II$_{opt}$ subtraction.

Column (3).—Equivalent width of Hβ (broad component only).

Column (4).—Uncertainty of Hβ equivalent width at a 2 σ confidence level.

Column (5).—FWHM(Hβ_{BC}) in Å; the value is as derived from the Hβ_{BC} profile measurements reported in Table 4.

Column (6).—Continuum level at λ4861 in units of 10^{-15} ergs s^{-1} cm^{-2} Å^{-1}. This means that the specific flux has been

TABLE 3

SPECTROPHOTOMETRIC MEASUREMENTS

IAU (1)	S/N (2)	W^a $H\beta_{BC}$ (3)	ΔW^a $H\beta_{BC}$ (4)	FWHM^a $H\beta_{BC}$ (5)	$f_\lambda{}^b$ 4861 Å (6)	Flag (7)	$W_{min}{}^a$ Fe II λ4570 (8)	W^a Fe II λ4570 (9)	FWHM^a Fe II λ4570 (10)	ΔFWHM^a Fe II λ4570 (11)	W^a He II λ4686 (12)	FWHM^a He II λ4686 (13)	$f_\lambda{}^b$ 4686 Å (14)	W^a $H\beta_{NC}$ (15)	W [O III] λ5007 (16)	$f_\lambda{}^b$ λ5007 (17)	W^a He II $\lambda4686_{NC}$ (18)
J00059+1609	45	118.0	10.0	84.9	2.110	0	11.0	17.0	107.19	12.13	24.1	101.0	2.342	3.50	32.50	1.916	1.0
J00063+2012	39	94.0	9.0	30.0	5.932	0	5.0	26.2	29.54	4.04	21.6	98.0	5.504	4.30	24.20	6.159	3.7
J00105+1058	43	164.0	16.0	79.4	1.401	0	7.0	54.0	78.88	12.13	−1.0	−1.0	1.449	7.70	78.00	1.369	2.3
J00196+2602	25	95.5	9.0	66.7	1.502	0	18.0	28.0	50.57	4.04	3.6	21.0	1.637	2.23	47.70	1.389	−1.0
J00292+1316	47	71.7	7.0	37.0	1.571	0	10.0	20.0	34.40	8.09	3.0	15.0	1.604	3.00	27.70	1.515	1.8
J00457+0410	20	101.0	11.0	79.4	0.637	0	20.0	75.0	70.79	16.18	−1.0	−1.0	0.679	−1.00	0.00	0.620	−1.0
J00470+0319	14	120.0	20.0	88.6	0.989	0	20.0	23.0	58.66	40.44	−1.0	−1.0	1.238	1.30	28.00	0.820	−1.0
J00495+1128	31	108.0	11.0	36.3	0.508	0	10.0	30.3	91.01	28.31	4.0	25.0	0.553	5.10	36.70	0.462	−1.0
J00519+1725	13	166.0	17.0	91.2	0.482	0	20.0	17.0	−1.00	−1.00	10.0	18.0	0.486	19.00	104.00	0.480	3.0
J00535+1241	70	46.1	5.0	17.7	7.147	0	5.0	60.0	18.22	−1.00	−1.0	−1.0	7.421	−1.00	15.30	6.923	−1.0
J00548+2525	33	164.6	16.0	88.8	1.501	0	14.0	24.0	99.10	12.13	−1.0	−1.0	1.609	6.50	54.00	1.418	1.0
J00573−2222	35	45.9	6.0	17.4	16.800	0	10.0	25.0	18.22	4.04	12.0	106.0	18.360	−1.00	7.40	15.310	−1.0
J00586−3606	39	90.6	9.0	81.5	1.499	0	11.0	33.0	66.75	12.13	9.0	100.0	1.627	1.80	8.80	1.393	1.4
J01032+0221	12	130.0	20.0	102.8	240.400	−1	25.0	26.0	−1.00	−1.00	34.0	84.0	258.300	4.00	22.00	219.20	1.2
J01138+1316	19	110.0	15.0	66.8	0.814	0	17.0	49.0	62.70	8.09	10.0	28.0	0.809	11.80	123.00	0.821	1.2
J01237−5848	40	110.8	10.0	101.6	2.977	0	14.0	47.6	74.84	12.13	−1.0	−1.0	3.036	7.50	62.10	2.931	2.4
J01315−2222	11	60.0	10.0	77.8	0.431	0	22.0	14.0	−1.00	−1.00	−1.0	−1.0	0.434	6.00	32.90	0.430	5.0
J01364+2057	9	250.0	50.0	92.2	0.130	0	80.0	64.7	382.18	−1.00	60.0	90.0	0.151	−1.00	186.00	0.116	−1.0
J01402−0050	29	159.0	18.0	86.9	0.992	0	14.0	26.0	−1.00	−1.00	9.7	97.0	1.064	−1.00	22.00	0.941	−1.0
J01402−2214	31	151.0	15.0	78.8	1.633	0	18.0	54.0	78.88	16.18	42.1	131.0	1.722	9.34	75.00	1.584	2.1
J01419+3923	21	98.4	10.0	230.4	0.619	0	35.0	49.0	208.29	40.44	−1.0	−1.0	0.600	0.91	60.00	0.636	−1.0
J01576−1043	10	112.0	10.0	66.7	0.380	0	27.0	37.0	58.66	16.18	40.0	80.0	0.424	11.00	137.00	0.347	−1.0
J01598+0023	37	66.4	8.0	49.7	1.206	0	11.0	38.0	46.53	12.13	−1.0	−1.0	1.320	6.90	54.40	1.102	4.1
J02022−7620	20	93.0	5.0	113.2	0.618	0	22.0	13.0	192.11	−1.00	−1.0	−1.0	0.645	3.50	34.00	0.595	1.0
J02078+0242	34	49.7	10.0	23.3	3.198	0	10.0	15.4	34.40	8.09	6.4	53.0	3.419	2.70	25.00	3.015	−1.0
J02145−0046	48	86.0	8.0	42.7	12.020	0	10.0	15.9	50.57	−1.00	94.4	374.0	12.040	1.89	16.20	11.990	1.8
J02174−0308	19	113.0	6.0	75.0	0.528	0	15.0	44.0	54.62	20.22	10.0	66.0	0.577	2.80	13.80	0.495	−1.0
J02346−0847	28	98.0	10.0	121.5	2.770	0	17.0	25.0	99.10	44.48	−1.0	−1.0	2.904	6.00	58.00	2.668	3.2
J02449+6228	20	90.0	15.0	228.0	0.492	−1	45.0	65.0	220.42	60.66	−1.0	−1.0	0.414	7.00	18.20	0.554	−1.0
J03118−5532	23	115.0	8.0	94.9	0.637	0	18.0	27.0	74.84	20.22	10.0	100.0	0.682	−1.00	8.10	0.609	−1.0
J03181−3426	51	107.0	9.0	114.2	1.488	0	11.0	37.0	99.10	20.22	6.1	123.0	1.604	2.10	16.10	1.390	−1.0
J03198+4130	55	22.0	−1.0	91.8	4.082	−1	−1.0	0.0	−1.00	−1.00	16.0	122.0	4.166	21.00	124.00	4.033	1.4

NOTE.—Table 3 is available in its entirety in the electronic edition of the *Astrophysical Journal Supplement*. A portion is shown here for guidance regarding its form and content.

[a] Rest frame equivalent width in Å.

[b] Rest frame specific flux in units of 10^{-15} ergs s^{-1} cm^{-2} Å^{-1}. J01032+0221, J04136+1112, J06300+6905 have arbitrary intensity scale.

TABLE 4

Hβ_{BC} Line Profile Measurements

IAU (1)	f_{Peak}[a] (2)	f/f_{Peak} (3)	λ_B[b] (4)	$\Delta^-\lambda_B$[b] (5)	$\Delta^+\lambda_B$[b] (6)	λ_R[b] (7)	$\Delta^-\lambda_R$[b] (8)	$\Delta^+\lambda_R$[b] (9)	f/f_{Peak} (10)	λ_B[b] (11)	$\Delta^-\lambda_B$[b] (12)	$\Delta^+\lambda_B$[b] (13)	λ_R[b] (14)	$\Delta^-\lambda_R$[b] (15)	$\Delta^+\lambda_R$[b] (16)	f/f_{Peak} (17)	λ_B[b] (18)	$\Delta^-\lambda_B$[b] (19)	$\Delta^+\lambda_B$[b] (20)
J00059+1609	2.38	0.00	4728.00	20.54	20.54	5064.80	38.21	38.21	0.25	4799.74	10.73	3.11	4940.39	4.85	7.28	0.50	4822.35	6.20	3.04
J00063+2012	13.28	0.00	4773.10	26.29	26.29	4975.20	42.77	42.77	0.25	4833.48	5.17	3.35	4885.65	3.82	5.31	0.50	4844.86	1.64	1.52
J00105+1058	2.65	0.00	4761.91	8.23	8.23	4980.33	6.79	6.79	0.25	4811.00	3.75	3.24	4923.73	4.14	4.68	0.50	4826.67	2.81	2.73
J00196+2602	1.60	0.00	4751.42	37.82	37.82	5037.76	33.84	33.84	0.25	4815.68	3.99	3.31	4911.67	4.67	23.88	0.50	4829.46	2.40	2.35
J00292+1316	1.76	0.00	4790.16	10.26	10.26	4976.40	22.83	22.83	0.25	4833.97	6.66	5.33	4905.05	3.75	7.20	0.50	4849.24	1.61	1.42
J00457+0410	0.56	0.00	4704.92	28.05	28.05	4947.00	27.09	27.09	0.25	4789.47	12.34	7.74	4907.66	2.70	2.70	0.50	4812.54	3.07	2.98
J00470+0319	0.98	0.00	4705.10	−1.00	−1.00	5022.44	1.65	1.65	0.25	4753.63	8.58	17.73	4942.71	8.03	8.45	0.50	4808.11	9.50	6.73
J00495+1128	0.98	0.00	4782.65	12.76	12.76	4963.90	17.47	17.47	0.25	4832.31	3.69	2.98	4887.83	1.93	2.48	0.50	4843.82	1.60	1.35
J00519+1725	0.74	0.00	4734.78	21.62	21.62	5091.73	85.75	85.75	0.25	4801.71	4.11	3.85	4931.35	7.17	10.81	0.50	4818.65	2.94	2.75
J00535+1241	11.34	0.00	4793.32	13.79	13.79	4910.52	6.70	6.70	0.25	4842.46	4.56	2.78	4876.49	3.10	3.30	0.50	4850.90	1.24	1.27

λ_R[b] (21)	$\Delta^-\lambda_R$[b] (22)	$\Delta^+\lambda_R$[b] (23)	f/f_{Peak} (24)	λ_B[b] (25)	$\Delta^-\lambda_B$[b] (26)	$\Delta^+\lambda_B$[b] (27)	λ_R[b] (28)	$\Delta^-\lambda_R$[b] (29)	$\Delta^+\lambda_R$[b] (30)	f/f_{Peak} (31)	λ_B[b] (32)	$\Delta^-\lambda_B$[b] (33)	$\Delta^+\lambda_B$[b] (34)	λ_R[b] (35)	$\Delta^-\lambda_R$[b] (36)	$\Delta^+\lambda_R$[b] (37)
4907.30	3.74	3.74	0.75	4840.81	4.28	2.18	4880.87	4.45	3.91	0.90	4847.02	2.00	2.00	4867.40	4.57	4.56
4874.81	1.14	1.23	0.75	4851.74	1.27	1.26	4869.64	1.03	1.00	0.90	4855.82	1.46	1.76	4866.30	1.54	1.18
4906.07	2.63	2.73	0.75	4839.90	2.22	1.92	4883.10	3.27	9.69	0.90	4845.44	1.82	2.11	4872.62	9.96	4.20
4896.13	2.17	2.27	0.75	4841.53	2.55	2.72	4885.42	2.33	2.19	0.90	4850.68	3.42	4.29	4877.58	3.77	2.94
4886.25	2.11	3.29	0.75	4855.05	1.02	1.02	4877.35	2.03	1.78	0.90	4858.35	1.21	1.51	4870.34	2.66	2.61
4891.93	3.13	3.65	0.75	4828.38	3.44	3.61	4880.82	1.63	1.66	0.90	4840.48	4.64	18.75	4875.68	2.24	1.82
4896.74	5.07	6.81	0.75	4829.86	3.20	3.19	4878.25	2.90	2.91	0.90	4840.09	3.69	4.57	4869.01	4.06	3.31
4880.18	1.21	1.26	0.75	4849.42	1.00	1.02	4874.35	1.21	1.15	0.90	4852.80	1.25	1.67	4870.29	2.11	1.51
4909.86	2.90	2.91	0.75	4831.98	2.67	2.79	4891.48	5.84	4.97	0.90	4841.18	3.40	4.16	4873.16	6.69	6.33
4868.62	0.70	0.81	0.75	4856.33	0.89	0.74	4865.53	0.58	0.56	0.90	4858.60	0.79	0.89	4863.77	0.91	0.58

Note.—Table 4 is available in its entirety in the electronic edition of the *Astrophysical Journal Supplement*. A portion is shown here for guidance regarding its form and content.

[a] Rest frame specific flux in units of 10^{-15} ergs s^{-1} cm^{-2} Å^{-1} save in the cases of J01032+0221, J04136+1112, J06300+6905 whose intensity scale is arbitary.

[b] Wavelength in Å.

multiplied by a factor $(1+z)^3$ when redshift correction was applied to the wavelength scale of each spectrum.

Column (7).—A flag identifying spectra that suffered extraordinary light losses, or whose scale is not in specific flux units (-1). A flag of value "0" means no known problem.

Column (8).—Fe II λ4570 upper limit in Å. This value can be considered a 3 σ estimate of the W(Fe II λ4570) uncertainty.

Column (9).—Fe II λ4570 equivalent width. The range of integration is between 4434 and 4684 Å, as in Boroson & Green (1992). This number is significant *only* if it is larger than the W(Fe II λ4570) lower limit for detection given in column (8). No measurement uncertainty is given for W(Fe II λ4570) since it can be deduced from the W(Fe II λ4570) upper limit: 2/3 of the upper limit value reported in column (8) can be an estimate of the error at a 2 σ confidence level. Errors are usually $\pm$20% at a 2 σ confidence level if W(Fe II λ4570) $\gtrsim W_{\rm UL}$(Fe II λ4570) of Figure 3.

Column (10).—FWHM(Fe II λ4570), in Å. The FWHM(Fe II λ4570) was measured with the scaling and broadening method and adopting a FWHM(Fe II λ4570) of I Zw 1 equal to 1100 km s^{-1}.

Column (11).—The error associated to FWHM(Fe II λ4570). A value of -1 means that FWHM(Fe II λ4570) is actually undetermined.

Column (12).—Equivalent with of He II λ4686 broad component, in Å.

Column (13).—FWHM(He II $\lambda 4686_{\rm BC}$) in Å.

Column (14).—Continuum specific flux at λ4686 in units of 10^{-15} ergs s^{-1} cm^{-2} Å^{-1}.

Column (15).—$W(\rm H\beta_{NC})$.

Column (16).—W([O III] λ5007).

Column (17).—Continuum specific flux at λ5007 in units of 10^{-15} ergs s^{-1} cm^{-2} Å^{-1}.

Column (18).—$W(\rm He\ II\ \lambda 4686_{NC})$; Unavailable values are labeled "-1."

We do not provide FWHM of narrow lines since their values are strongly affected by instrumental broadening. In general, negative values ($-1.$) indicate a high uncertain value or that a parameter could not be measured.

In spectra where we were unable to detect Fe II$_{\rm opt}$ emission, we set an upper limit for W(Fe II λ4570) according to the appropriate S/N and expected line width. This procedure will enable to treat nondetections as censored data. In such cases, an Fe II$_{\rm opt}$ best fit was still subtracted (the Fe II$_{\rm opt}$ emission shown in Fig. 4), but its influence on the H$\beta_{\rm BC}$ profile estimates is well within the observational errors.

H$\beta_{\rm BC}$ *Profiles*.—Measurements of the cleaned H$\beta_{\rm BC}$ profile are presented in Table 4. These profiles have been measured applying a FORTRAN program to an high-order spline fitting of the H$\beta_{\rm BC}$ (as done by Marziani et al. 1996). Spline fits are visible as thick lines in the right panels of Figure 4. The format of Table 4 is as follows:

Column (1).—IAU source designation.

Column (2).—Peak intensity, in units of 10^{-15} ergs s^{-1} cm^{-2} Å^{-1} (exceptions noted in § 2.1).

Columns (3)–(9).—At fractional intensity 0 (col. [3]), wavelength of line blue side (col. [4]) with lower and upper uncertainties (cols. [5] and [6]); wavelength of line red side (col. [7]) with lower and upper uncertainties (cols. [8] and [9]).

Columns (10)–(16).—Same line parameters as for columns (3)–(9), evaluated at fractional intensity 1/4.

Columns (17)–(23).—Same line parameters as for columns (3)–(9), evaluated at fractional intensity 1/2.

Columns (24)–(30).—Same line parameters as for columns (3)–(9), evaluated at fractional intensity 3/4.

Columns (31)–(37).—Same line parameters as for columns (3)–(9), evaluated at fractional intensity 0.9.

Uncertainties were estimated assuming that the main sources of error involve continuum placement plus H$\beta_{\rm BC}$ and H$\beta_{\rm NC}$ decomposition. The errors were therefore computed as the line wavelength measured at $i/4 \pm 0.05$ fractional intensity level minus the measured wavelength, i.e.,

$$\Delta\lambda^{\pm}_{B,R}(i/4) = \lambda_{B,R}(i/4 \pm 0.05) - \lambda_{B,R}(i/4)\ .$$

Note that this assigns asymmetric errors save at $i = 0$, where the errors are assumed symmetric and equal to the ones obtained assuming $\lambda_{B,R}(i/4 \pm 0.05)$.

5.3. *General Trends*

BLR origin of Fe II$_{\rm opt}$.—The assumption of FWHM equality for (H$\beta_{\rm BC}$) and (Fe II λ4570) can be tested a posteriori within ΔFWHM $\approx$ 20%. In sources where Fe II λ4570 was weak or undetected, it was impossible to measure W(Fe II λ4570). In such cases we give an upper limit for the W(Fe II λ4570) and no measurements for FWHM(Fe II λ4570) in Table 3 (-1 code value). We were able to measure FWHM(Fe II λ4570) for 135 objects, and these data allowed us to directly test the hypothesis that broad-line emission from Fe II$_{\rm opt}$ and H$\beta_{\rm BC}$ arise in the same region. We confirm that FWHM(Fe II λ4570) and FWHM(H$\beta_{\rm BC}$) are highly correlated (see, e.g., Phillips 1978, and Boroson & Green 1992 for landmark studies). Individual Fe II template fits are rather insensitive to the adopted broadening factor (which is affected by large errors), but the statistical distribution of FWHM Hβ versus FWHM Fe II λ4570 is much more sensitive to a systematic difference. The FWHM(H$\beta_{\rm BC}$) $\approx$ FWHM(Fe II λ4570) assumption is verified for sources with FWHM Hβ $<$ 4000 km s^{-1}. Broader sources suggest that FWHM(H$\beta_{\rm BC}$) is systematically larger than FWHM(Fe II λ4570). The FWHM difference between these lines that is found only for population B objects is not a random error but a systematic difference possibly due to the presence of the extra VBLR component in Hβ.

An important result of this investigation is that the Fe II$_{\rm opt}$ template based on I Zw 1 provides a good fit, within the limits imposed by S/N, for almost every of the 215 objects in our sample. In one case (J22032+3145) the Fe II$_{\rm opt}$ emission may be markedly different. Even this single example is doubtful because the Fe II λ4570 emission was not observed and the peculiarity is apparent only in the Fe II$_{\rm opt}$ λ5230 blend. Mrk 231 (J12562+5652) is a source with apparently peculiar Fe II$_{\rm opt}$ emission; however, it shows heavy internal extinction, with $A_V \approx 2.0$. In Figure 4, the red Fe II$_{\rm opt}$ blend appears to be depressed relative to Fe II λ4570, but since the fit was based on Fe II λ4570, it is in reality the converse: the internal extinction is able to significantly depress the Fe II λ4570 emission that is $\approx$250 Å blueward. IRAS 07598+6508 shows an apparent Fe II$_{\rm opt}$ emission width *significantly* narrower than the Hβ. IRAS 07598+6508 and Mrk 231 are both outliers in the E1 parameter space. We note, however, that the Fe II$_{\rm opt}$ template reproduces satisfactorily the Fe II λ4570 emission in both cases.

Dependence of E1 parameters on luminosity.—The relevance of any redshift incompleteness to eigenvector 1 studies depends on how strongly the E1 parameters [i.e., FWHM(Hβ_{BC}) and $R_{Fe\ II}$] depend upon L. The evidence up to this time suggests that any correlation is absent in the luminosity range covered by our data: correlating FWHM(Hβ_{BC}) and $R_{Fe\ II}$ with M_B yields Pearson's correlation coefficient -0.1 and 0.06, respectively. A direct answer at $M_B \lesssim -30$ involves observation of the Hβ spectral range in higher redshift quasars. We are in the process of obtaining good S/N VLT spectra of the Hβ region out to $z \sim 2.5$.

Variability.—How robust are our line measures in the face of the tendency for many AGN to vary widely? Our own experience, and results in the literature, suggest that most line profiles keep the same basic shape in response to considerable continuum change (see, e.g., Corbin & Smith 2000). Exceptions are few although notable (e.g., Sulentic et al. 2000b). The best response is to say that the range of profile changes likely falls within the large range of profile types that are observed. That is, after all, why it is so important to obtain high-quality spectra for a large number of sources—to adequately sample the phenomenology. Our sample incorporates the PG database of $n = 87$ mostly RQ quasars kindly provided by the authors (Boroson & Green 1992). Many of these sources have been reobserved as our sample was expanded, especially in the direction of sources with suitable matching C IV λ1549 data in the *HST* archive (see Marziani et al. 1996 for analysis of the first 52 sources and Sulentic et al. 2000c for a more recent analysis of 127 sources). It is possible to compare spectra for reobserved sources to look for evidence of temporal changes in line profiles. In Table 5 we report a log of observations for objects that were observed more than once:

Column (1).—IAU code name.

Column (2).—Common name.

Column (3).—Observing date.

Column (4).—Universal Time at exposure start.

Column (5).—Exposure time in seconds.

Column (6).—Observing date. The date refers to the spectrum reported in Table 2 and plotted in the atlas (Fig. 4) if on the first table row of any object.

Column (7).—Universal Time at exposure start, as for column (6).

Column (8).—Exposure time in seconds, as for column (7).

Column (9).—This column flags the object according on whether there was (1) no evidence for strong Hβ_{BC} profile variation (N), (2) positive evidence (Y), or (3) variation was possible but confirming data are needed (P). Note that the flag refers an analysis of the spectra listed in Table 5 *only*.

Column (10).—Comment on the variation and a reference if the source is known for variability.

No object showed remarkable changes in the line profiles that may not have been discussed previously. We found variations in objects that have been extensively studied: for instance, NGC 4151 (Ulrich 2000 and references therein), PG 1416−129 (Sulentic et al. 2000b), B2 1512+370 (Romano, Marziani, & Dultzin-Hacyan 1998). The role of variability in the E1 parameter space will be discussed in a companion paper.

Weak Hβ_{BC}.—A few borderline cases for which W(Hβ_{BC}) is rather small have been considered. Some objects could be transient undergoing strong line changes (see NGC 4151 and PG 1416−129; see also below). Other objects may have only a "very broad-line component" which would be a dangerous source of confusion in statistical studies. We suggest that 3C 232 (J09583+3224) is a prototypical case. In that source FWHM(Hβ_{BC}) = 13,000 km s^{-1} and W(Hβ_{BC}) $\approx$ 45 Å, unusually low for a population B, radio-loud source. It is not a unique case as 3C 110, and B2 1721+34 show similar spectra. Other low-W(Hβ_{BC}) sources show profiles similar to that of 3C 232, but with a prominent narrower core (still too broad to be attributed to Hβ_{NC}: for example, J09466+0725. These objects resemble PG 1416−129, which has undergone a strong continuum change (Sulentic et al. 2000b) and subsequent quenching of the classical BLR emission. As a result, it is possible that only the innermost very broad component, and emission a few light years away from the continuum sources, are likely sources of broad-line emission. Considering the profile of Hβ, it is very unlikely that these objects are radio-loud NLSy1's, as recently suggested (see, e.g., PKS 2004−447; Oshlack, Webster, & Whiting 2001).

In one case, NGC 1275, Hβ_{BC} may be almost completely absent. The width of He II λ4686 suggests, however, that

TABLE 5

OBJECTS WITH REPEATED OBSERVATIONS

IAU Code Name (1)	Common Name (2)	Obs. Date (3)	U.T. (4)	Exp. Time (s) (5)	Obs. Date (6)	U.T. (7)	Exp. Time (8)	Flag (9)	Notes (10)
J00059+1609	PKS 0003+15	1990 Oct 19	06:50	3000	1996 Oct 14	04:02	3600	P	Hβ_{BC} red wing change?
J00059+1609	PKS 0003+15	1995 Jun 29	10:51	2400					
J00063+2012	Mrk 335	1990 Sep 18	06:10	500	1996 Oct 13	04:02	3000	N	
J00063+2012	Mrk 335	1995 Jun 01	02:39	3600					
J00105+1058	III Zw 2	1990 Sep 18	06:24	1200	1994 Oct 08	02:07	5400	N	
J00105+1058	III Zw 2	1995 Jul 01	09:50	3600					
J00457+0410	PG 0043+039	1994 Oct 09	02:57	6000	1990 Sep 20	05:44	2700	N	
J00535+1241	I Zw 1	1990 Sep 19	07:48	600	1994 Oct 07	04:11	5400	N	
J00535+1241	I Zw 1	1996 Oct 14	04:54	2700					
J00548+2525	PG 0052+251	1990 Oct 18	06:29	1800	1994 Dec 09	03:39	3600	N	

NOTE.—Table 5 is available in its entirety in the electronic edition of the *Astrophysical Journal Supplement*. A portion is shown here for guidance regarding its form and content.

broad-line emission is indeed present. We have provided an $H\beta_{BC}$ component fit, but its merit is merely indicative.

6. CONCLUSIONS

We present spectra for the Hβ spectral region in 215 AGNs including 77 RL sources. While RL are overrepresented, we suggest that this sample may be large enough to reasonably characterize AGN broad-line phenomenology at least in low-redshift sources. The spectral atlas reveals an impressive spectroscopic diversity. This suggests that average quasar spectra are likely to have physical meaning only if this diversity is taken into account (Sulentic et al. 2002). We discuss possible sample and spectroscopic measurement biases. We also consider the major properties that affect the reproducibility of the measurements including the presence/absence of an NLR component in the narrowest profiles and the certain presence of an additional redshifted very broad component (VBLR) in the broader profiles.

Despite its biases, our sample is very useful for a tests and analysis of the E1 parameter space, especially since both FWHM($H\beta_{BC}$) and $R_{Fe\ II}$ do not show any appreciable dependence on source luminosity. Another major result is the robustness of the I Zw 1 Fe II$_{opt}$ spectrum as a template for fitting optical Fe II emission for any line width and strength. Comparison of the FWHM values adopted for the Fe II$_{opt}$ template subtraction with the FWHM($H\beta_{BC}$) measures confirms the likelihood of a common origin for the two lines. The discovery that $H\beta_{BC}$ is broader than Fe II λ4570 in population B sources is likely connected with the extra VBLR component associated with Hβ.

P. M., R. Z., M. C., and R. B. acknowledge financial support from the Italian MURST through Cofin 00-02-004. D. D.-H. acknowledges grant IN 115599 PAPIIT-UNAM.

REFERENCES

Bennert, N., Falcke, H., Schulz, H., Wilson, A. S., & Wills, B. J. 2002, ApJ, 574, L105
Boroson, T. 2002, ApJ, 565, 78
Boroson, T. A., & Green, R. F. 1992, ApJS, 80, 109
Collin-Souffrin, S., Dyson, J. E., McDowell, J. C., & Perry, J. J. 1988, MNRAS, 232, 539
Corbin, M. R., & Smith, P. S. 2000, ApJ, 532, 136
Ferland, G. J. 2000, Rev. Mexicana Astron. Astrofis. Ser. Conf., 9, 153
Gaskell, C. M. 1982, ApJ, 263, 79
Grupe, D., Beuermann, K., Mannheim, K., & Thomas, H.-C. 1999, A&A, 350, 805
Hooper, E. J., Impey, C. D., Foltz, C. B., & Hewett, P. C. 1995, ApJ, 445, 62
Kellermann, K. I., Sramek, R., Schmidt, M., Shaffer, D. B., & Green, R. 1989, AJ, 98, 1195
Marziani, P., Sulentic, J. W., Calvani, M., Perez, E., Moles, M., & Penston, M. V. 1993, ApJ, 410, 56
Marziani, P., Sulentic, J. W., Dultzin-Hacyan, D., Calvani, M., & Moles, M. 1996, ApJS, 104, 37
Marziani, P., Sulentic, J. W., Zwitter, T., Dultzin-Hacyan, D., & Calvani, M. 2001, ApJ, 558, 553
Nagao, T., Murayama, T., & Taniguchi, Y. 2001, ApJ, 546, 744
Oshlack, A. Y. K. N., Webster, R. L., & Whiting, M. T. 2001, ApJ, 558, 578
Peterson, B. M., & International AGN Watch. 2002, ApJ, in press
Phillips, M. M. 1978, ApJS, 38, 187
Romano, P., Marziani, P., & Dultzin-Hacyan, D. 1998, ApJ, 495, 222
Shapovalova, A. I., et al. 2001, A&A, 376, 775
Sulentic, J. W., Marziani, P., & Dultzin-Hacyan, D. 2000a, ARA&A, 38, 521
Sulentic, J. W., Marziani, P., Dultzin-Hacyan, D., Calvani, M., & Moles, M. 1995, ApJ, 445, L85
Sulentic, J. W., Marziani, P., Zamanov, R., Bachev, R., Calvani, M., & Dultzin-Hacyan, D. 2002, ApJ, 566, L71
Sulentic, J. W., Marziani, P., Zwitter, T., Dultzin-Hacyan, D., & Calvani, M. 2000b, ApJ, 545, L15
Sulentic, J. W., Zwitter, T., Marziani, P., & Dultzin-Hacyan, D. 2000c, ApJ, 536, L5
Ulrich, M.-H. 2000, Astron. Astrophys. Rev., 10, 135
Urry, C. M., & Padovani, P. 1995, PASP, 107, 803
Véron, P., Gonçalves, A. C., & Véron-Cetty, M.-P. 2002, A&A, 384, 826
Véron-Cetty, M.-P., & Véron, P. 2000, A Catalogue of Quasars and Active Nuclei (Garching: ESO)
Zamanov, R., Marziani, P., Sulentic, J. W., Calvani, M., Dultzin-Hacyan, D., & Bachev, R. 2002, ApJ, 576, L9
Zheng, W., & Sulentic, J. W. 1990, ApJ, 350, 512